SIAM J. Appl. Math.
Vol. 84, No. 2, pp. 477–496

STEADY WIND-GENERATED GRAVITY-CAPILLARY WAVES ON VISCOUS LIQUID FILM FLOWS*

Y. MENG†, D. T. PAPAGEORGIOU†, AND J.-M. VANDEN-BROECK‡

Abstract. Steady gravity-capillary periodic waves on the surface of a thin viscous liquid film supported by an air stream on an inclined wall are investigated. Based on lubrication approximation and thin air-foil theory, this problem is reduced to an integro-differential equation. The small-amplitude analysis is carried out to obtain two analytical solutions up to the second order. Numerical computation shows there exist two distinct primary bifurcation branches starting from infinitesimal waves, which approach solitary wave configuration in the long-wave limit when the values of physical parameters are above certain thresholds. New families of solutions manifest themselves either as secondary bifurcation occurring on primary branches or as isolated solution branches. The limiting configurations of the primary solution branches with the increase of two parameters are studied in two different cases, where one and two limiting configurations are obtained, respectively. For the latter case, the approximation of the configurations is given.

Key words. thin films, air/liquid flows, gravity-capillary waves

MSC codes. 76A20, 68R10, 68U05

DOI. 10.1137/23M1586318

1. Introduction.

Gas sheared thin film flows arise in a number of natural phenomena and technological applications, e.g., cooling of electronic devices, mass transfer in distillation columns, and falling film flows in nuclear fusion reactors. Research has been conducted on instabilities leading to wave formation with the objective of understanding fundamental mechanisms and their utilization in the optimization of processes using gas-liquid film flow. An important area of applications involves gas-driven flow regime transitions in gas-liquid flows in pipes and channels [14]; large-amplitude solitary type waves have been linked to the phenomenon of flooding that can significantly degrade process performance. It is important, therefore, to model and analyze such fundamental phenomena using appropriate mathematical models to understand the system's solutions. It is a first and crucial step in designing passive and active control protocols—for the control of liquid film flows see, for example, [4, 15, 16].

Hanratty and Engen [7] explored experimentally the interaction between a turbulent air stream and a water liquid film and documented the different wave transition regimes. As the gas flow rate increased, the initially smooth liquid surface successively gave way to two-dimensional (2D) waves, squalls, roll waves, and dispersed flows. Hanratty and Hershman [8] extended the theory of Jeffreys and Taylor [9] to account for the initiation of roll waves in the concurrent flows of a turbulent air

---

*Received by the editors July 12, 2023; accepted for publication (in revised form) January 2, 2024; published electronically March 21, 2024.

https://doi.org/10.1137/23M1586318

Funding: The work of the first author was funded by a Roth Scholarship in Mathematics, Imperial College London. The work of the second author was partly funded by Engineering and Physical Sciences Research Council (EPSRC) grant EP/V062298/1.

†Department of Mathematics, Imperial College London, London, SW7 2AZ, UK (y.meng22@imperial.ac.uk, d.papageorgiou@imperial.ac.uk).

‡Department of Mathematics, University College London, London, WC1E 6BT, UK (j.vanden-broeck@ucl.ac.uk).

and liquid. The theoretical predictions were compared with the experimental data for different types of liquid solutions, and good agreement was found. Craik [5] performed experiments on a uniform thin liquid film on a horizontal flat plate in the presence of airflow. Under constant gas flow, "slow" and "fast" waves were observed. The "slow" waves traveled with speeds smaller than that of the liquid surface and were nonperiodic with steep fronts and long rears. The "fast" waves were distinctly sinusoidal and traveled faster than the liquid surface. Demekhin [6] assumed the gas-liquid interface as a rigid fixed wavy wall and then treated the problem in the turbulent gas separately. An integral-boundary-layer model was developed in the long-wave limit and numerical computations of steady periodic waves were carried out. They found "trough" type near-soliton solutions for a sufficiently small wave-number. Jurman and McCready [10] observed 2D steady periodic waves when the gas velocity was above the neutral stability value, and for sufficiently large gas Reynolds number, steady solitary waves appeared. However, these waves broke into 3D periodic waves at larger gas velocities. To describe the observed waves, these authors derived a weakly nonlinear equation and performed linear stability analysis to understand the kinematic or dynamic process in different regimes. Peng, Jurman, and McCready [13] experimentally compared the wave fields observed at low and high liquid Reynolds numbers. Their results showed that at lower liquid Reynolds numbers, solitary waves appeared as a secondary transition from existing waves having large-amplitude-substrate depth ratios. If the fluid layer is too thick, large-amplitude-substrate depth ratios cannot be achieved and this transition to solitary waves does not occur. They also speculated that the degree of dispersion plays an important role in the formation of large precursor waves (to solitary waves).

King and Tuck [11] considered a viscous fluid layer supported by steady airflow on an inclined wall and reduced this problem to an integro-differential equation based on the lubrication approximation for the liquid flow and thin air-foil theory for the driving gas flow [21]. Below a critical wall inclination angle, two distinct drop-shaped solutions were obtained numerically. It is worth noting that surface tension was confined to the region close to the leading edge of the fluid layer and neglected elsewhere. For the same physical setup, King, Tuck, and Vanden-Broeck [12] used a similar integro-differential equation model to study steady spatially periodic gravity waves in the absence of surface tension. An analytical solution was obtained using small-amplitude analysis to show some typical features of the waves. Periodic waves with finite amplitudes were computed numerically, and a limiting solitary wave configuration was found by increasing the wavelength to indicate the existence of air-driven gravity solitary waves on the film. Tseluiko and Kalliadasis [17] established various asymptotic models to describe the dynamics of falling liquid films on an inclined wall in the presence of turbulent airflow. Traveling wave solutions were computed numerically based on the integral-boundary-layer model, and the change of amplitudes and velocities of these waves confirmed the existence of large-amplitude stationary waves, which are believed to corresponded to the onset of flooding.

The related problem of the formation of hydraulic bores has been considered by [1], [2] in the case of inviscid flows and by [3] for viscous flow models having arbitrary Reynolds number. Bore solutions are constructed in different regimes and in some cases multiple states are found to co-exist.

In the present paper, we extend the results of [12] by including the effect of surface tension and investigate the wave configurations fully. The structure of the paper is as follows. A brief derivation of the model equation is give in section 2. The small-amplitude theory analysis is carried out, and a complete analytical solution is then obtained in section 3. In section 4 we compute various bifurcations, wave profiles in different cases, and limiting configurations of the periodic waves in relevant limits of the physical parameters. Finally, section 5 is devoted to the conclusion.

2. Formulation.

The physical model of a 2D flow is depicted in Figure 1. A Newtonian fluid with constant density ρ and viscosity μ flows under gravity along a flat substrate which is inclined to the horizontal direction at an angle α. We shall assume $\alpha < \pi/2$ in the following analysis; for vertical plates the scalings are slightly different. An upward air stream with constant density ρ_A flows over the fluid with speed u_A. The viscosity of the air region is neglected. A Cartesian coordinate system (x, y) is introduced where the x-axis points up the substrate as shown in Figure 1 and y is perpendicular to it with $y = 0$ on the substrate. The film thickness is $y = h(x, t)$ and its undisturbed value is h_0. The liquid-air surface tension coefficient is σ and the acceleration due to gravity is denoted by g.

The upward air stream exerts both a tangential and a normal stress on the liquid film. We assume that the tangential stress is constant with a known drag coefficient C_D while the pressure is determined by the shape of the fluid layer by thin air-foil theory [21]. As a result, the following evolution equation for the fluid layer is readily obtained after a standard long-wave formulation:

$$h_t + \frac{1}{3\mu}\left[\left(\rho_A u_A^2 \mathcal{H}[h_{xx}] - \rho g h_x \cos\alpha - \rho g \sin\alpha + \sigma h_{xxx}\right) h^3 + \frac{3\rho_A u_A^2 C_D}{4} h^2\right]_x = 0, \tag{2.1}$$

where $\mathcal{H}$ is the Hilbert transform defined as

$$\mathcal{H}[g](x) = \frac{1}{\pi} \fint_{-\infty}^{\infty} \frac{g(\xi')\mathrm{d}\xi'}{x - \xi'}, \tag{2.2}$$

where the Cauchy principal value of the integral is implied. Formal derivations of (2.1) have been given by [20] and [12] (see also [19]). The equation is nondimensionalized using the following scalings:

$$\tilde{x} = x/\lambda, \qquad \tilde{h} = y/h_c, \qquad \tilde{t} = t/T_c,$$

where λ is the wavelength of wave solutions. Tildes represent dimensionless variables. The scalings for wave height and time are

$$h_c = \frac{\rho_A u_A^2 C_D}{2\rho g \sin\alpha}, \qquad T_c = \frac{6\mu\lambda}{\rho g h_c^2 \sin\alpha}. \tag{2.3}$$

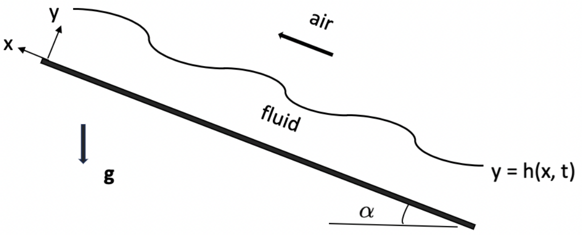

Fig. 1. *Schematic of the problem and coordinate system.*

These are obtained by considering positive constant solutions when the flux is positive, namely when the upstream air flow is inducing a net flux up the substrate against gravity—see [12] for details. In addition, the value h_c in (2.3) is chosen so that the convective terms in the linear problem cancel. After some algebra and dropping tildes yields

$$\frac{1}{2}h_t + \left[\left(\frac{\nu^2}{d_1}\fint_{-\infty}^{\infty}\frac{h''\mathrm{d}\xi}{x-\xi} + \frac{\nu^3}{d_2}h_{xxx} - \nu h_x - 1\right)h^3 + 3h^2/2\right]_x = 0, \tag{2.4}$$

where the dimensionless parameters are

$$\nu = \frac{h_c}{\lambda\tan\alpha}, \qquad d_1 = \frac{\pi C_D}{2\tan^2\alpha}, \qquad d_2 = \frac{\rho g h_c^2\sin\alpha}{\sigma\tan^3\alpha}. \tag{2.5}$$

Note that the parameter d_1 in (2.5) includes the π factor from the Hilbert transform definition (2.2). The parameter ν is inversely proportional to the size of the system (if $\nu \ll 1$ the wavelengths are asymptotically large), d_1 measures the induced drag, and d_2 is a scaled Bond number based on h_c.

The steady form of (2.4) is integrated once to yield

$$\frac{3}{2h} + \frac{\nu^2}{d_1}\frac{\mathrm{d}}{\mathrm{d}x}\fint_{-\infty}^{\infty}\frac{h_\xi\mathrm{d}\xi}{x-\xi} + \frac{\nu^3}{d_2}h_{xxx} - \nu h_x - 1 = \frac{q}{h^3}, \tag{2.6}$$

where q is the flux of fluid in the positive x direction, and we will be concerned with solutions to (2.6). For $\sigma = 0$, i.e., $d_2 \to \infty$, (2.6) degenerates to the equation obtained by [12].

Before proceeding with our study of (2.6), we comment on the unsteady version in order to motivate the inclusion of surface tension. A spatially uniform steady state of (2.4) is $h = H_0$, and linearizing about this and looking for normal mode solutions proportional to $e^{ikx+2st}$ gives

$$s = -\nu k^2 + \frac{\nu^2\pi}{d_1}k^2|k| - \frac{\nu^3}{d_2}k^4, \tag{2.7}$$

from which we can see that in the absence of surface tension ($d_2 \to \infty$) the linear problem is short-wave unstable and hence the initial value problem is ill-posed. Interestingly, an identical linear dispersion relation arises in wave formation on a perfectly conducting falling liquid film at Reynolds numbers below critical, when there is a vertical electric field (uniform far away) acting in the air region above the liquid film—see [18]. If the Reynolds number is above critical, then the $-\nu k^2$ term becomes νk^2, hence adding to the instability present due to the Hilbert transform term.

3. Weakly nonlinear theory.

In this section, we seek asymptotic solutions of (2.6) in the small-amplitude regime. We consider a constant film height solution of $h(x) = h_0 > 0$ with constant flux $q = q_0$. Using (2.6) it follows that

$$q_0 = h_0^2\left(\frac{3}{2} - h_0\right). \tag{3.1}$$

It follows from (3.1) that there are two nonzero film height solutions for $0 < q_0 < 1/2$, one solution for $q_0 < 0$, and a single critical solution $h_0 = 1$ when $q_0 = 1/2$. In what follows we develop a weakly nonlinear theory to study the bifurcated solutions from the critical point $q_0 = 1/2$, $h_0 = 1$. The parabolic form of the h_0 versus q_0 curve near this point implies that $q_0 - 1/2 \sim (h_0 - 1)^2$. Introducing the ordering $|h-1| \sim \epsilon \ll 1$ implies the asymptotic expansions

$$h = 1 + \epsilon h_1 + \epsilon^2 h_2 + \epsilon^3 h_3 + \cdots, \tag{3.2}$$

$$q = \frac{1}{2} + \epsilon^2 q_2 + \epsilon^3 q_3 + \cdots, \tag{3.3}$$

$$\nu = \nu_0 + \epsilon \nu_1 + \epsilon^2 \nu_2 + \epsilon^3 \nu_3 + \cdots. \tag{3.4}$$

Substituting (3.2)–(3.4) into (2.6), we find at $O(\epsilon)$

$$\frac{\nu_0^2}{d_1} \frac{\mathrm{d}}{\mathrm{d}x} \fint_{-\infty}^{\infty} \frac{h_1^{'} \mathrm{d}\xi}{x - \xi} + \frac{\nu_0^3}{d_2} h_{1xxx} - \nu_0 h_{1x} = 0. \tag{3.5}$$

Without loss of generality, we then take $h_1 = a\cos(2\pi x) + b$ where a and b are constants, a solution with unit period, which leads to

$$\nu_0 = \frac{\pi d_2 \pm \sqrt{(\pi d_2)^2 - 4 d_1^2 d_2}}{4\pi d_1}. \tag{3.6}$$

Equation (3.6) indicates the existence of two branches of solutions since given admissible parameters d_1 and d_2 we can have two real values of ν_0. We call these two branches an *upper branch,* corresponding to the positive sign yielding larger ν_0 and shorter waves, and a *lower branch* corresponding to the negative sign representing longer waves. For small surface tension $d_2 \to \infty$, and the upper branch has the limiting form $\nu_0 \to \infty$. The lower branch in this limit has $\nu_0 = d_1/(2\pi^2)$ in full agreement with the result in the gravity case [12].

Equation (3.6) gives real solutions if $d_2 \geq 4d_1^2/\pi$. Complex solutions when $d_2 < 4d_1^2/\pi$ reflect the fact that no nontrivial steady states exist then. This can be seen from the growth rate (2.7) by taking $k = 2\pi$ to match the analysis in this section and rewriting

$$s = -\frac{(2\pi)^4 \nu}{d_2} \left[\left(\nu - \frac{d_2}{4d_1} \right)^2 + \frac{d_2}{4\pi^2} - \frac{d_2^2}{16 d_1^2} \right]. \tag{3.7}$$

It follows that $s < 0$ whenever $d_2 < 4d_1^2/\pi$; hence the waves are linearly stable and the only steady states are the uniform ones.

Proceeding to the next order, we find

(3.8)

$$\frac{\pi \nu_0^2}{d_1} \mathcal{H}[h_{2xx}] + \frac{\nu_0^3}{d_2} h_{2xxx} - \nu_0 h_{2x} = \frac{3}{2} h_1^2 - \frac{2\nu_0 \nu_1}{d_1} \mathcal{H}[h_{2xx}] - \frac{3\nu_0^2 \nu_1}{d_2} h_{1xxx} + \nu_1 h_{1x} + q_2.$$

To guarantee the wavelike property of solutions, we remove secular terms by choosing $b = 0$, $q_2 = -\frac{3a^2}{4}$, and $\nu_1 = 0$. The solution for h_2 is

$$h_2 = e\cos 2\pi x + f + g \sin 4\pi x, \tag{3.9}$$

where

$$G = \frac{3a^2 d_1 d_2}{64 d_2 \pi^3 \nu_0^2 - 256 d_1 \pi^3 \nu_0^3 - 16\pi d_1 d_2 \nu_0},$$

which degenerates to $3\pi a^2/8d_1$ as $d_2 \to \infty$ for the lower branch. The coefficients e and f are determined at $O(\epsilon^3)$ and we find

$$e = 0, \quad f = \frac{a^2}{8}, \quad \nu_2 = \frac{3gd_1d_2}{48\nu_0^2\pi^3 d_1 + 4\pi d_1 d_2 - 16\pi^3\nu_0 d_2}.$$

Up to the second order, the solution of (2.6) is

$$h = 1 + \left[\frac{4}{3}\left(\frac{1}{2} - q\right)\right]^{1/2}\cos 2\pi x + \frac{1-2q}{12}\left(1 + \frac{3\sin 4\pi x}{8d_2\pi^3\nu_0^3 - 32d_1\pi^3\nu_0^3 - 2\pi d_1 d_2\nu_0}\right), \tag{3.10}$$

and

$$\nu = \nu_0 + \cdots, \tag{3.11}$$

where ν_0 is given by (3.6). From the asymptotic analysis, two different branches of solutions are obtained. The lower branch agrees with the results in the gravity case as $d_2 \to \infty$. Both solution branches exist when q is slightly smaller than 1/2 and are completely determined by prescribing d_1, d_2, and q. At leading order, the wavelength (specified by ν) is only dependent on d_1 and d_2. It is also worth noting that the wave solutions are asymmetric about $x = 0$. These weakly nonlinear features determine the form of the solution in the subsequent nonlinear numerical computation.

In the above analysis the solution is taken to be unimodal with unit period. Denoting this solution by $h(x;\nu)$, it can be readily seen from (2.6) that given a positive integer $M \geq 2$, then $h_M := h(Mx;\nu/M)$ is also a solution at the same values of the flux q and the parameters d_1 and d_2. This observation allows us to construct multimodal states from the unimodal branches. For example, we can obtain the bimodal wave branch by using the linear unimodal results as an initial guess but with ν decreased by a factor of 2. This is used to initialize our computations when multimodal branches are computed.

4. Numerical methods and results.

4.1. Numerical method.

We explore the solutions of (2.6) numerically. In light of the asymmetry of the asymptotic solutions, we write the solution as the truncated Fourier series

$$h(x) = a_0 + \sum_{n=1}^{N} a_n\cos(2\pi nx) + b_n\sin(2\pi nx), \tag{4.1}$$

where $a_0 \neq 0$ is the mean film height, and we can select $b_1 = 0$ by a shift of origin since the problem is Galilean invariant. We note also that using the fact that $\mathcal{H}[\cos x] = \sin x$ and $\mathcal{H}[\sin x] = -\cos x$, we can express the Hilbert transform integral explicitly as

$$\frac{\nu^2}{d_1}\frac{\mathrm{d}}{\mathrm{d}x}\,⨍_{-\infty}^{\infty}\frac{h_\xi \mathrm{d}\xi}{x-\xi} = -\frac{4\pi^3\nu^2}{d_1}\left(\sum_{n=1}^{N} n^2\sin(2\pi nx) - n^2\cos(2\pi nx)\right). \tag{4.2}$$

All solutions presented here are periodic with period 1, and we term these unimodal. As we see below, such unimodal solutions can terminate in multimodal ones as parameters vary, or bifurcate from multimodal branches—we present examples for bimodal and trimodal structures but note that any modal state exists linearly and can be continued numerically.

As seen from (4.1), $2N$ real unknown Fourier coefficients are introduced (a_0, $a_1,\dots,a_N$, and $b_2,\dots,b_N$). In addition ν and q are unknown but dependent (for example, we can fix q and compute ν as part of the solution, using continuation thereafter). Hence, $2N+1$ unknowns are needed to solve (2.6). This requires $2N+1$ collocation points $x_i = i/(2N+1), i = 0,1,2,\dots,2N$, to close the system. Newton's method is used to solve the resulting nonlinear algebraic system for given values of d_1 and d_2. The initial guess for Newton's method comes from the weakly nonlinear solutions presented above. In every iteration the Jacobian matrix is calculated analytically prior to each iteration. Iterations are terminated when the error is less than 10^{-10}, thus guaranteeing accurate results. Several numerical experiments were carried out to determine the truncation N, with the conclusion that $N = 250$ gives sufficiently accurate solutions. Therefore, in the computations that follow we choose $N = 250$.

We begin our computations by fixing the two physical parameters d_1 and d_2, which represent the effect of airflow and surface tension, respectively. To guarantee real ν in linear initializations of the system, it follows from (3.11) that we need to satisfy $d_2 > 4d_1^2/\pi^2$. Therefore, we only focus on the parameter region where $d_2 > 4d_1^2/\pi^2$ in the numerical computations that follow.

4.2. Bifurcations and wave profiles.

As discussed above, there are two branches of solutions emerging from the linear and weakly nonlinear results—see (3.6). In what follows we compute nonlinear solutions and bifurcations for these branches and investigate their interactions as the parameters d_1 and d_2 vary. To illustrate the nature of the solutions we fix $d_1 = 0.8$ and compute solutions as d_2 is increased above the value $d_2 = 4d_1^2/\pi^2$ which is required for the existence of linear and weakly nonlinear solutions. For $d_1 = 0.8$ this value is $d_2 \approx 0.2594$. Once the quantitative features of the solutions are described, we produce a numerically constructed phase diagram that delineates solution branches in the $d_1 - d_2$ phase space—see Figure 7.

4.2.1. The case $d_1 = 0.8$ and $d_2 = 0.313$.

We begin by presenting results for the upper branch with $d_1 = 0.8$ and $d_2 = 0.313$. In Figure 2(a), a representative collection of bifurcation diagrams is plotted in the 3D phase space (q, A, ν), where A is the computed wave amplitude. All branches appear to asymptotically approach limiting solutions as ν tends to zero, i.e., the wavelength tends to infinity. The almost limiting solutions marked by the circles on the curves in Figure 2(a) are shown in Figure 2(d), with the flux q decreasing from top to bottom. These waves approach "hump" type solitary waves as $\nu \to 0$. The solitary wave with the smallest flux (bottom plot in panel (d)) possesses more ripples on the left side compared to the other two profiles. While the behavior as $\nu \to 0$ is similar, the three bifurcation curves shown in Figure 2(a) start with different periodic waves as depicted in panel (c). The top branch denoted as the unimodal primary branch originates from infinitesimal waves, and its bifurcation mechanism is analogous to the gravity wave cases shown in [12].

Additional bifurcation branches exist besides the primary branch. It can be seen that the second branch (dashed red curve) and third branch (dotted yellow curve) start with waves of finite amplitude, shown in Figure 2(c), which emerge from the bimodal and trimodal primary branches (note that the starting waves in the second and third plots of Figure 2(c) are *almost* bimodal and trimodal, respectively). Hence, new families of solutions appear as secondary finite-amplitude bifurcations from the points on multimodal primary branches. Figure 2(b) shows the projection of the 3D bifurcation curves into (q, ν) space, where the solid blue and dashed red curves correspond to the branches of the same colors in Figure 2(a). The green dash-dot curve

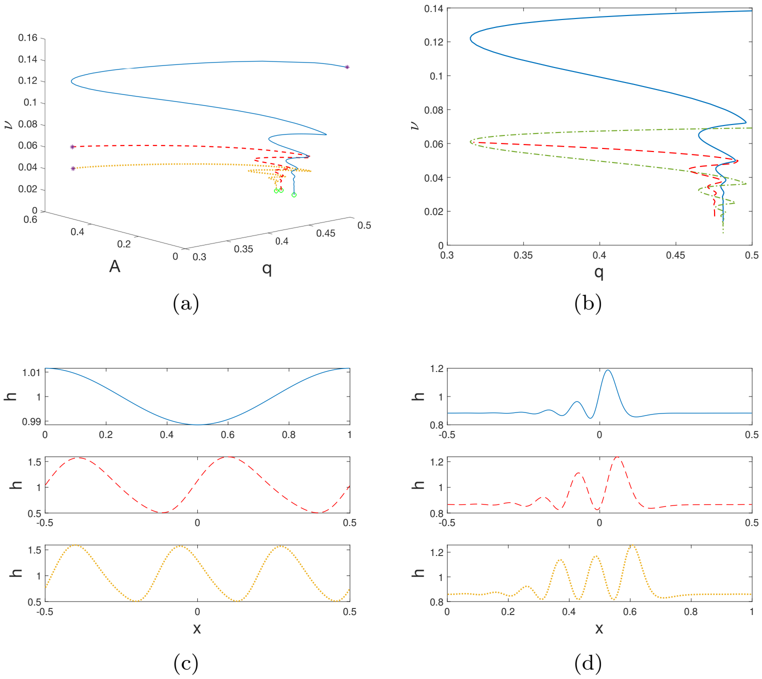

Fig. 2. *Bifurcation diagrams and typical profiles of upper branches for $d_1 = 0.8$ and $d_2 = 0.313$.* (a) *The unimodal primary bifurcation branch (solid blue) and secondary bifurcation branches (dashed red, dotted yellow) from bimodal, trimodal primary branches.* (b) *The projection of 3D bifurcations onto (q, ν) space. The solid blue and dashed red curves correspond to the branches with the same colors and line types in Figure* 2(a)*; the dash-dot green curve represents the branch originating from infinitesimal bimodal waves.* (c) *Wave profiles of the starting points (labeled by stars) on the bifurcation curves.* (d) *Wave profiles of the ending points (labeled by circles) on the bifurcation curves. (Color online.)*

is the projection of the 3D bifurcation starting from infinitesimal bimodal waves (not shown in panel (a)), the shape of which is the same as that of the unimodal primary branch after the scaling $\nu \to \nu/2$, as explained at the end of section 3. It can be seen that the dashed red curve just emanates from the first turning point of the dash-dot bimodal curve. It is interesting to note that the second and third bifurcation curves start with waves of almost the same flux q, and corresponding values of $\nu \approx 0.0607$ and 0.0406, respectively, which are consistent with the scaling predictions in section 3. In summary, the three bifurcation diagrams shown for $d_1 = 0.8$ and $d_2 = 0.313$ start with unimodal, bimodal, and trimodal waves, respectively, and terminate with similar limiting waves of different flux. It should be emphasized that we have only presented three representative upper branch bifurcation curves for $d_1 = 0.8$ and $d_2 = 0.313$. However, there exist more solutions which branch off from other multimodal waves and approach solitary wave configurations as $\nu \to 0$. For example, the fourth branch is expected to start from tetramodal waves with $\nu \approx 0.03$ and end with a solitary wave configuration which has more ripples compared to the wave profile on the bottom of Figure 2(d).

We now turn to the lower branch solutions for $d_1 = 0.8$, $d_2 = 0.313$. Results are shown in Figures 3(a)–3(d). The top branch (solid blue curve) in Figure 3(a) bifurcates from infinitesimal unimodal waves; the results show that it does not approach a

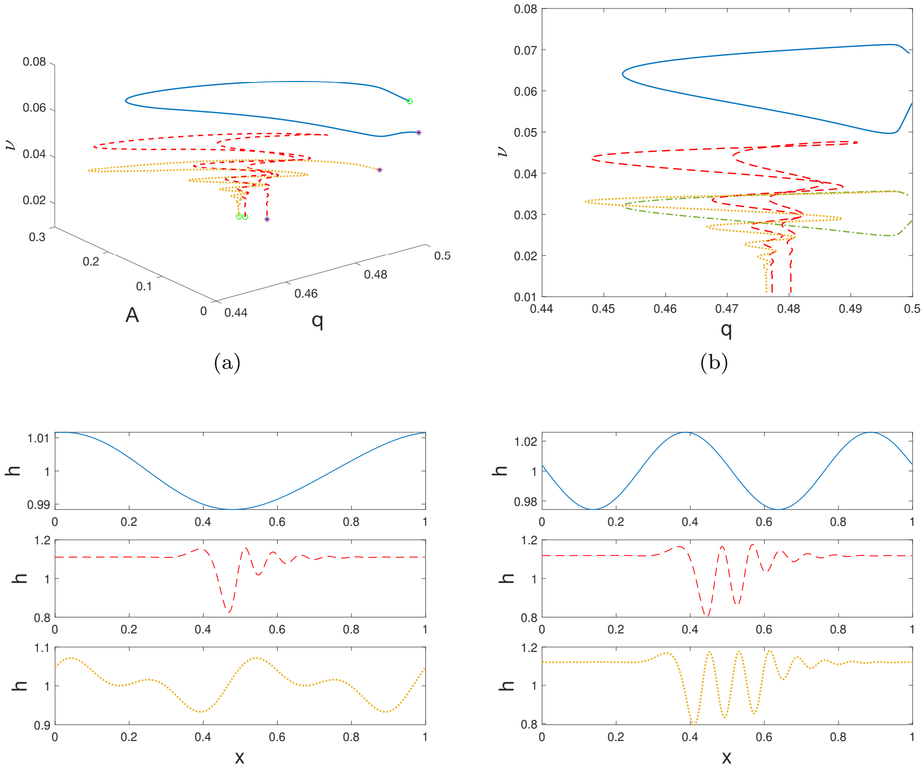

(a) (b)

(c) (d)

FIG. 3. *Bifurcation diagrams and typical profile of lower branches for* $d_1 = 0.8$ *and* $d_2 = 0.313$. (a) *The unimodal primary bifurcation branch (solid blue), a new isolated branch (dashed red), and a secondary bifurcation branch (dotted yellow) from bimodal primary branch.* (b) *The projection of 3D bifurcations onto* (q, ν) *space. The curves correspond to the branches in the same colors and line types in* (a)*, while the dash-dot line represents the bimodal primary branch.* (c) *Wave profiles of the starting points (labeled by stars) on the bifurcation curves.* (d) *Wave profiles of the ending points (labeled by circles) on the 3D bifurcation curves.*

solitary wave as is the case for the upper branch, and instead terminates with linear bimodal waves—see the top plots (solid blue curves) in Figures 3(c) and 3(d) for the starting points marked with a star and the end points marked with a circle. The second branch at lower values of ν (the dashed red curve) appears to be an isolated branch connecting two "trough" type solitary waves with different fluxes as $\nu \to 0$; these are shown in the middle plots of Figures 3(c) and 3(d). The solitary wave with smaller flux (panel (d)) also features more ripples, which is a characteristic of upper branch solitary waves presented earlier. The last dotted bifurcation curve included in Figure 3(a) and shown in yellow branches off from a finite-amplitude wave on the bimodal primary branch and eventually produces a solitary wave as $\nu \to 0$. Figure 3(b) shows the projection of the 3D bifurcation curves in Figure 3(a), as well as the branch bifurcating from infinitesimal bimodal waves represented by the dash-dot green line. It is clear from panel (b) that the dotted yellow branch is connected with the bimodal primary bifurcation by a secondary bifurcation point—see also the bottom (dotted yellow) plot of Figure 3(c), which shows the starting profiles to be nonlinear and bimodal. The numerical results show that there are two different solitary wave

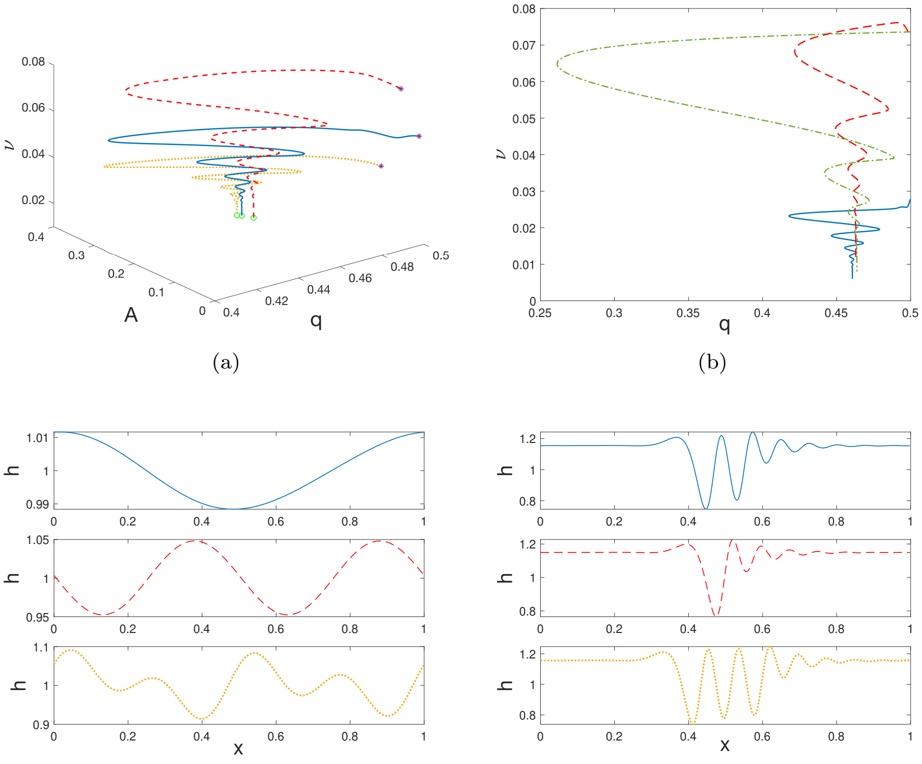

(a) (b)

(c) (d)

FIG. 4. *Bifurcation diagrams and typical profiles of lower branches for* $d_1 = 0.8$ *and* $d_2 = 0.325$. (a) *The unimodal primary bifurcation branch (solid blue) and secondary bifurcation branches from bimodal waves.* (b) *The projection of* 3D *bifurcations onto* (q, ν) *space. The curves correspond to the branches with the same colors and line types in* (a), *while the dash-dot line represents the bimodal primary branch.* (c) *Wave profiles of the starting points (labeled by stars) on the bifurcation curves.* (d) *Wave profiles of the ending points (labeled by circles) on the* 3D *bifurcation curves.*

configurations corresponding to the upper and lower branches, that is, the "hump" type solitary waves with ripples on the left and the "trough" type solitary waves with ripples on the left. A qualitative analogy to these two kinds of configurations is the elevation and depression solitary waves in water wave theory.

4.2.2. The case $d_1 = 0.8$ and $d_2 = 0.325$. Next we keep $d_1 = 0.8$ and increase d_2 to 0.325. The behavior described next is similar for larger values of d_2 also—we are above a critical value that produces solitary waves for all computed branches as $\nu \to 0$. A phase diagram in $d_1 - d_2$ space is constructed later after we illustrate details of the solutions. The upper branches are qualitatively similar to the case $d_1 = 0.313$ and so the results are not included here. The lower branches are different, however. The new feature is that the unimodal primary branch (shown by the solid blue curve in Figure 4(a)) approaches a solitary wave configuration as $\nu \to 0$, unlike termination to a linear bimodal state as found for $d_1 = 0.313$—see Figure 3(a). In general we find that as d_2 is increased (for a fixed d_1), the upper primary branch produces a solitary wave as $\nu \to 0$ at a lower value of d_2 than the value required for the lower primary branch to terminate in a solitary wave. We also notice that the other two bifurcations (the dashed red and dotted yellow curves in Figure 4(a)) branch out from secondary points on primary branches and tend to solitary waves as the wavelength approaches infinity. It can be seen from Figure 4(b) that the dashed red unimodal curve bifurcates from a point on the branch starting with infinitesimal bimodal waves (the dash-dot green line). The starting wave profiles identified by stars in Figure 4(a) are given in Figure 4(c), while the ending solitary waves denoted by open circles are given in Figure 4(d); the same color scheme is used in all panels.

4.2.3. The case $d_1 = 0.8$ and $d_2 = 0.31, 0.3$. In the third numerical experiment, we choose $d_1 = 0.8$ and $d_2 = 0.31$, a value closer to the critical one, $d_2 \approx 0.2594$. Figure 5(a) shows three representative bifurcation curves for the upper branches. The unimodal primary branch (solid blue curve) emanates from infinitesimal waves and ends with a bimodal wave of finite amplitude shown in the top plot of Figure 5(d). This indicates that the upper primary branches cannot approach solitary waves when d_2 is below a critical value. The second bifurcation is a separated branch which links two "hump" type solitary waves at its two end points—see the middle plots in dashed

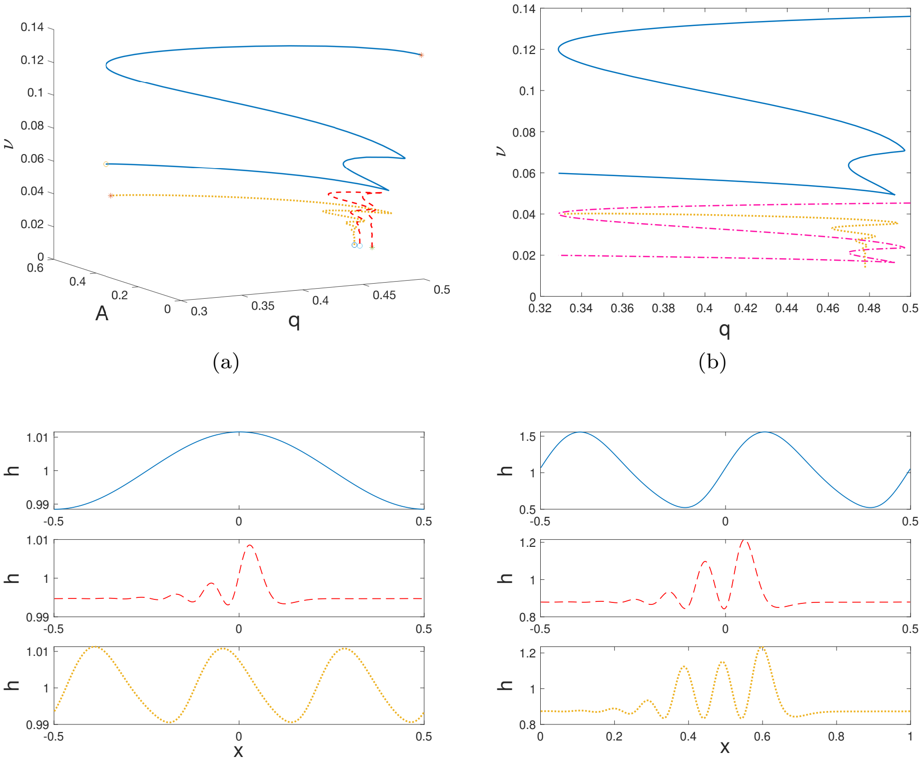

(a) (b)

(c) (d)

FIG. 5. *Bifurcation diagrams and typical profiles of upper branches for $d_1 = 0.8$ and $d_2 = 0.31$.* (a) *The unimodal primary bifurcation branch (solid blue), a new isolated branch, and a secondary bifurcation branch from the trimodal primary solution branch.* (b) *The projection of 3D bifurcations onto (q, ν) space. The curves correspond to the branches with the same colors and line types in* (a), *while the dashed line represents the trimodal primary branch.* (c) *Wave profiles of the starting points (labeled by stars) on the bifurcation curves.* (d) *Wave profiles of the ending points (labeled by circles) on the bifurcation curves.*

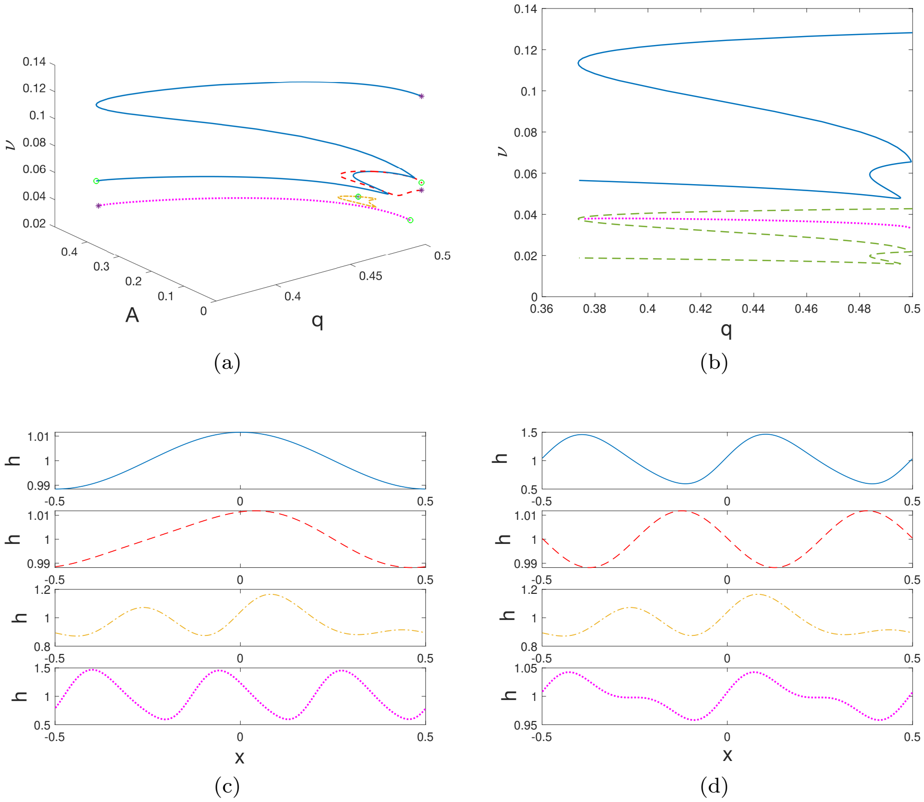

(a) (b)

(c) (d)

Fig. 6. *Bifurcation diagrams and typical profile of branches for* $d_1 = 0.8$ *and* $d_2 = 0.3$. (a) *Unimodal primary bifurcation curves for the upper (solid blue) and lower (dashed red) branch, a new isolated closed branch (dash-dot yellow), and a secondary bifurcation from trimodal primary branch.* (b) *The projection of* 3D *bifurcations onto* (q, ν) *space. The two curves correspond to the branches with the same colors and line types in* (a), *while the dashed line represents the trimodal primary branch.* (c) *Wave profiles of the starting points (labeled by stars) on the bifurcation curves.* (d) *Wave profiles of the ending points (labeled by circles) on the bifurcation curves.*

red in Figures 5(c) and 5(d). The bottom branch is a secondary bifurcation from the trimodal primary solution branch, which can be observed clearly from the projection of the 3D trajectories in Figure 5(a) into Figure 5(b). The profiles of the starting and ending points, labeled by the asterisks and circles, respectively, are shown in Figures 5(c) and 5(d). The lower branches are completely analogous to those described for the case $d_2 = 0.313$, and for brevity we exclude the results.

Next we decrease d_2 to the value 0.3, keeping $d_1 = 0.8$. No solitary waves were found by varying ν (see Figure 6(a)) for both upper and lower branches. From top to bottom in Figure 6(a), the first and second curves (blue and red, respectively) are the unimodal upper and lower primary branches; the former terminates with finite-amplitude bimodal waves while the latter one ends with infinitesimal bimodal waves. The third bifurcation (dash-dot yellow) is an isolated and closed branch. The last branch (dotted pink) bifurcates from a secondary point on the trimodal primary branch, which is shown by the dashed green curve in Figure 6(b), and is linked with a bimodal wave. Typical profiles labeled by circles and asterisks on the 3D bifurcation diagrams are shown in Figures 6(c) and 6(d).

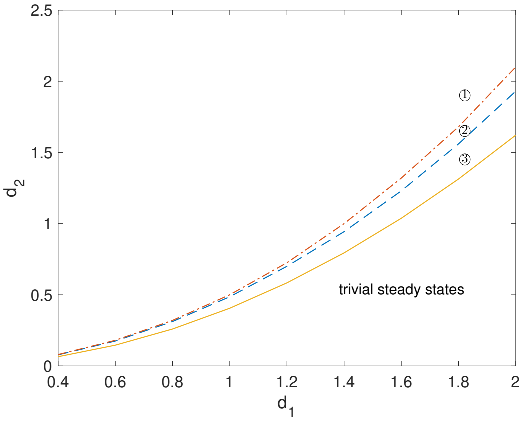

FIG. 7. *Regions of* $d_1 - d_2$ *space where solitary waves exist or not for primary branches. Region* 1: *both upper and lower primary branches can approach solitary waves as* $\nu \to 0$; *region* 2: *only the upper primary branches approach solitary waves as* $\nu \to 0$; *region* 3: *no solitary waves for both upper and lower branches as* $\nu \to 0$.

4.2.4. Solution phase diagram in (d_1, d_2) space. The results given for the fixed value $d_1 = 0.8$ as d_2 varies show a rich bifurcation structure of upper and lower branch solutions in (q, A, ν) space. It is noted that for $d_1 = 0.8$ there exist two critical values of d_2, namely $d_2 \approx 0.312$ and $d_2 \approx 0.32$, for the primary upper and lower branches, respectively, above which the bifurcation curves can approach solitary waves as $\nu \to 0$. Extensive computations were carried out to extend these canonical phenomena to a wide range of values of d_1. The results are given in Figure 7. The yellow solid line is given by $d_2 = 4d_1^2/\pi$ and denotes the boundary below which no steady state linear and weakly nonlinear solutions exist—see section 3. Hence, we focus on the region $d_2 > 4d_1^2/\pi$, which is itself divided into three regions numbered on the figure, and which are characterized as follows. For a given d_1, no solitary waves can be found for the primary branches when d_2 is in region 3. The primary upper branches arrive at solitary waves as $\nu \to 0$ when d_2 is located in region 2. Increasing the value of d_2 until it is in region 1, we find that both primary upper and lower branches can approach solitary waves as $\nu \to 0$. The boundaries between the regions were computed using continuation methods and monitoring the limits $\nu \to 0$.

Next, we take the upper bifurcation diagrams for $d_1 = 0.8$ and $d_2 = 0.313$ given in Figure 2 as an example to further explore the connection among different branches. It is shown in Figure 2(a) that the three branches depicted approach solitary waves with different values of q and A as $\nu \to 0$. This implies that we can find a discrete set of solitary waves through the continuation of ν for different solution branches. To find out whether there exist solitary waves for other values of q, for instance, for values of q between the circles on the blue and red curves, we explore the bifurcation curve in the (q, A) plane with fixed large wavelength determined by ν. The results are given in Figure 8 for $\nu = 0.014$ and $d_1 = 0.8$, $d_2 = 0.313$. The dot and asterisk on the curve correspond exactly to the almost-solitary waves bifurcating from the unimodal and bimodal branches labeled by circles in Figure 2(a). We can conclude that the solitary waves computed in Figure 2 are located on the same solution branch. In addition, there exist solitary waves for a large range of values of q. If we perform further computations along this 2D curve, we expect to find points which correspond to solitary waves that branch off from other multimodal waves. However, there may

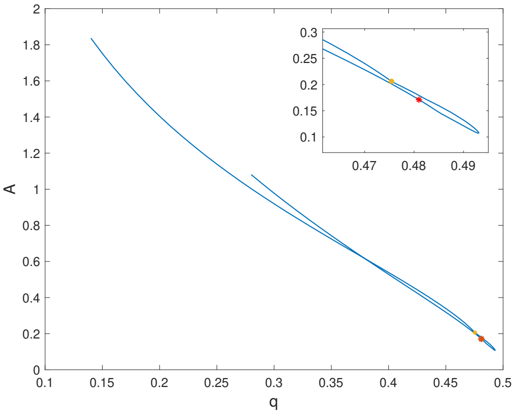

FIG. 8. *Bifurcation curves in* (q, A) *space with fixed* $\nu = 0.014$ *when* $d_1 = 0.8$ *and* $d_2 = 0.313$. *The dot and asterisk correspond to the two almost solitary waves on the unimodal primary branch (blue) and the secondary branch (red), respectively, in Figure* 2(a).

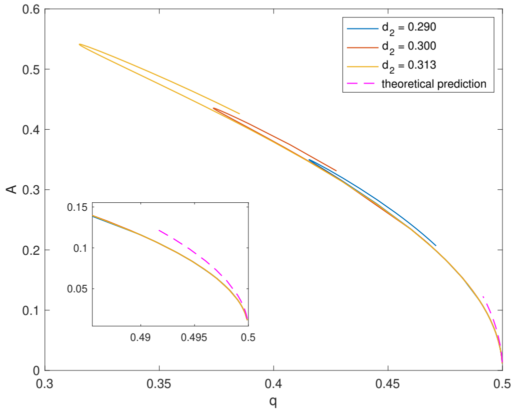

FIG. 9. *Plot of the amplitude* A *versus the flux* q *for various* d_2 *with* $d_1 = 0.8$.

exist many turning points before we arrive at the solutions. This is beyond the scope of our aims here, and we only present part of the bifurcation curve to illustrate the connection between the solitary waves bifurcating from unimodal and bimodal waves.

To explore the solution space further, we compute the variations of the wave amplitude A with the flux q for various values of d_2. We only focus on the branches originating from the infinitesimal unimodal waves at $q = 1/2$ for which we have small-amplitude asymptotic results given in section 3. Figure 9 shows the three upper branches for fixed $d_1 = 0.8$ and corresponding to $d_2 = 0.29, 0.3, 0.313$, respectively, as labeled on the figure. For these branches, the amplitude is predicted to be (see solution (3.10))

$$A = \frac{4}{3}\left(\frac{1}{2} - q\right)^{1/2}. \tag{4.3}$$

The prediction (4.3) is superimposed in Figure 9 with a dash-dot pink curve. Agreement of the theoretical prediction with the computations is seen to be good. As q moves away from 0.5, the waves become significantly nonlinear and the amplitudes dependent strongly on d_2 and q. It is worth noting that the curves shown in Figure 9 are intrinsically different from those in Figure 8. The curve in Figure 9 is the projection of the bifurcation curves from (A, q, ν) space onto the (q, A) plane. Therefore, the values of ν, and hence the wavelengths, of different points on the curve are different, while the bifurcation curve in Figure 8 represents a branch of wave solutions with the same wavelength. For every ν smaller than the value ν_0 prescribed by the small-amplitude theory, we can obtain a two-dimensional bifurcation curve which is a two-parameter branch determined by the wavelength and amplitude (or flux). However, the curve in Figure 2(a) is a single-parameter branch since both ν and $h(x)$ are specified by the flux q, as illustrated by the solutions in section 3. It should be noted that although some bifurcation diagrams in (A, q, ν) space do not directly start with infinitesimal waves, they are linked with the bifurcations starting with infinitesimal waves at a secondary bifurcation point. Therefore, in essence, these branches are still single-parameter branches.

4.2.5. Limiting configurations. King, Tuck, and Vanden-Broeck [12] considered waves in the absence of surface tension, i.e., when $d_2 = \infty$ in our notation. They found that as the wind parameter d_1 increases, which physically implies that the effect of the blowing is absent in the limit, the wave height as $|x| \to \infty$ of the long periodic waves (i.e., the height of the solitary wave tails) decreases and appears to tend to zero, signaling the formation of a drop solution. Therefore, they speculated that the periodic waves approach a series of separated blobs analogous to those studied by [11]. A complete exploration of this limit was not carried out and in what follows we do this and also consider the effects of surface tension.

The present study includes surface tension, and the small-amplitude theory in section 3 indicates that as $d_2 \to \infty$ (i.e., surface tension vanishes), the lower branch recovers the gravity wave solutions computed by King, Tuck, and Vanden-Broeck [12]. The asymptotic behavior of the upper branch is distinct in that the value of ν approaches infinity, yielding a singular limit in the sense that the wavelength decreases to zero. Note that this can be seen directly from the weakly nonlinear theory and the formula (3.11) with the plus sign that gives the upper branch. Therefore, we first focus on fixing d_1 and increasing the value of d_2. The results for $d_1 = 2$ are shown in Figure 10(a) for the behavior of the lower branch and Figure 10(b) for the upper branch. Figure 10(a) shows that as d_2 increases, the solution approaches the gravity wave solution computed in the absence of surface tension and superimposed in blue;

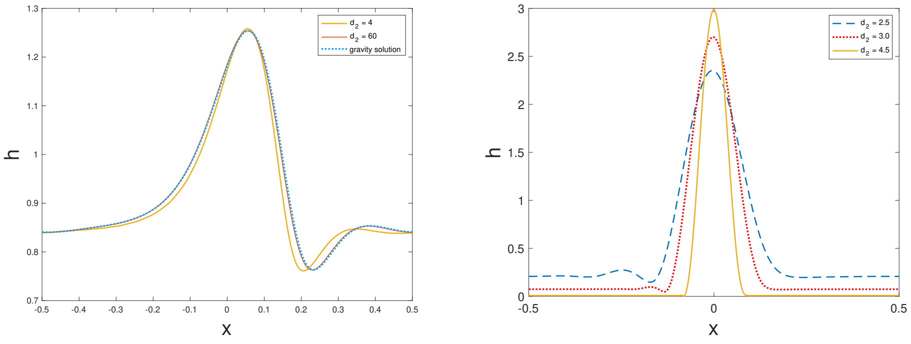

(a) (b)

FIG. 10. *Typical wave profiles on the lower and upper branches as* d_1 *is fixed to* 2 *and* d_2 *increases.* (a) *Comparison between wave profiles for various values of* d_2 *on the lower branch and the gravity solution.* (b) *Wave profiles with* $\nu = 0.15$ *for various* d_2 *on the upper branch.*

the difference between the $d_2 = 60$ and the $d_2 = \infty$ solutions is very small, as seen in the figure. Considering the upper branch results of Figure 10(b), we find that as d_2 increases, the wave thickness of the flat solitary wave tails decreases rapidly to small values, suggesting a touchdown. At the same time, the main part of the wave gets narrower. Note that this type of solution is strongly attracting since the wave almost touches the wall even for the moderate value of $d_2 = 4.5$. Note that in these computations we have fixed ν and varied d_2 in order to evaluate the effect of decreasing surface tension on waves having the same wavelength; this was also done by [12].

Next, we consider the limiting configurations when the air velocity parameter d_1 becomes large. As mentioned in section 3, to guarantee real ν and nontrivial steady states we must have $d_2 > 4d_1^2/\pi^2$, which in turn implies that $d_2 \to \infty$ as $d_1 \to \infty$. To explore this limit numerically, we pick $d_2 = d_1^3$ so as to guarantee nontrivial states for $d_1 \gg 1$. In the results that follow we retain surface tension (with the ordering $d_2 = d_1^3$) when computing the upper branch, but drop it when considering the lower branch solutions. This is motivated by the results in Figure 10(a); since $d_2 \gg d_1$ we recover the large d_1 gravity solutions of [12]. Here we construct solutions for larger values of d_1 than those considered by [12].

Figures 11(a) and 11(b) show typical wave profiles on the upper and lower branches, respectively, for various values of d_1 noted on the figures. As mentioned above, all lower branch solutions in Figure 11(b) are computed in the absence of surface tension. It can be seen that as d_1 increases, the flat portion of the waves moves closer to the substrate and the waves get narrower for both branches; this was also observed by [12] for gravity waves and values of $d_1 \leq 17$. At the same time, the wave profiles become almost symmetric about the origin. Results of the dependence on d_1 of the minimum wave height and the width of the corresponding profiles are given in Figure 12. We denote by hm_u and hm_l the minimum heights on the upper and the lower branch, respectively, and by w_u and w_l the corresponding wave profile widths defined to be the distance between the two almost symmetrically occurring minima. Figure 12(a) depicts the minima (the upper branch in a solid blue curve and the lower branch in a dashed red curve), and Figure 12(b) shows the corresponding variation in the wave widths. The data indicate that all four quantities decrease algebraically with d_1, and the exponents are given by the slopes of the curves in the log-log plots of Figure 12. Using least square fits we obtain, approximately,

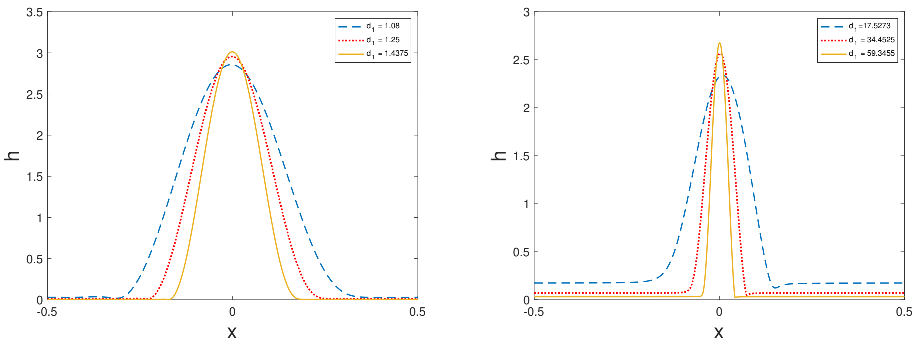

(a) (b)

FIG. 11. *Typical wave profiles for various d_1 with two values of ν.* (a) *Solutions on the upper branches for $\nu = 0.44$.* (b) *Solutions on the lower branches for $\nu = 0.3$.*

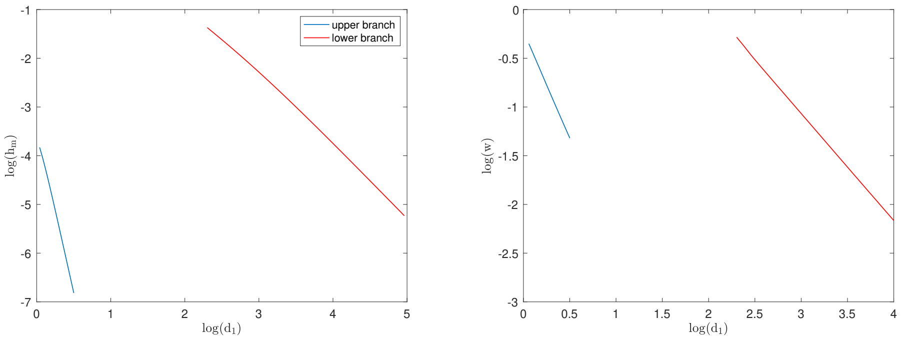

(a) (b)

FIG. 12. *Variation of the height of the lowest point from the substrate and the width of the profiles as d_1 tends to infinity.* (a) *Log-log plot of the height of the lowest point from the substrate and d_1.* (b) *Log-log plot of the width of the waves and d_1.*

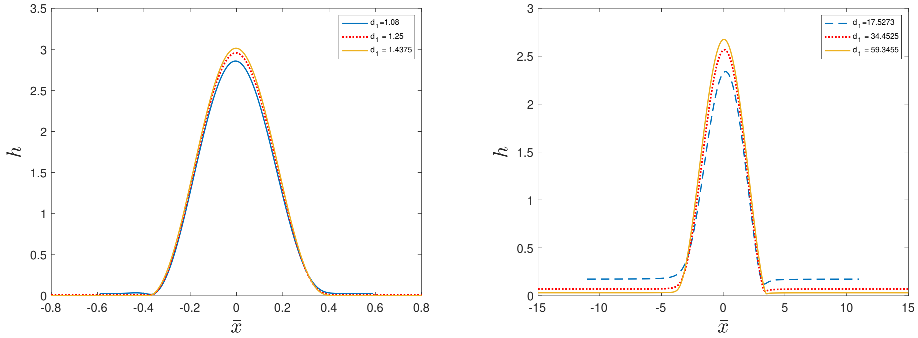

(a) (b)

FIG. 13. *Rescaled typical wave profiles for various values of d_1.* (a) *Solutions on the upper branch.* (b) *Solutions on the lower branches.*

$$hm_u = d_1^{-6.63}, \quad hm_l = d_1^{-1.49}, \qquad w_u = d_1^{-2.25}, \quad w_l = d_1^{-1.09}. \tag{4.4}$$

This indicates that according to the model, the limiting configuration cannot touch the bottom at a finite value of d_1, and so we cannot obtain the configuration of blobs computed by King and Tuck [11] unless additional physics is brought in and the models are modified to allow for dewetted solutions. In addition, the results presented here for limiting profiles (on both branches) as d_1 increases are found to converge to universal profiles under a spatial rescaling, as shown in Figure 13. We conclude this section by a closer analysis of the numerical results for the lower branch solutions in the absence of surface tension, i.e., in the limit $d_2 \to \infty$. To better identify the dominant characteristics of limiting configurations, we consider the relative sizes of the terms in (2.6) for the solution on the lower branch when $d_1 = 25.89$. In what follows we denote by T_1 the surface traction exerted by the air flow, i.e., the first term on the left-hand side (LHS) of (2.6). The pressure term induced by the air flow, i.e., the second term on the LHS of (2.6), is denoted by T_2. The gravity term $-\nu h_x$ is denoted by T_3, and finally the term $-q/h^3$ is denoted by T_4. The spatial dependence of these four terms is plotted together in Figure 14 and color coded as identified

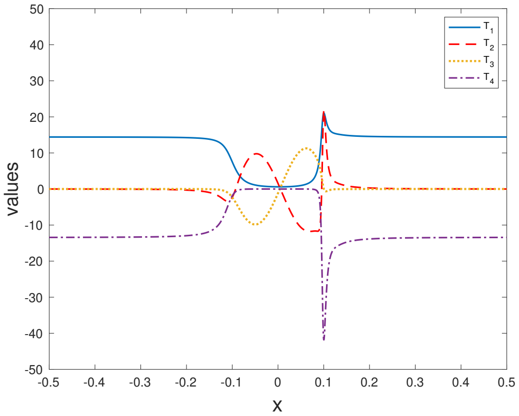

FIG. 14. *Plots of values of terms in* (2.6).

in the legend. Several conclusions can be drawn from the data in Figure 14. First, in the flat portion of the wave in the far field, the dominant terms are T_1 and T_4 so that the balance $q \sim \frac{3h^2}{2}$ follows. Second, close to the origin $x = 0$ where the main central part of the wave lies, it is seen from Figure 14 that the dominant balance is between the terms T_2 and T_3, i.e., a pressure-gravity balance yielding $(\nu^2/d_1)\mathcal{H}[h_{xx}] \sim \nu h_x$. Considering the almost symmetric feature of the limiting configuration, the center portion can be described as $a \cos Kx$, and the wave-number K can be determined by solving

$$\frac{\nu^2}{d_1}\mathcal{H}[h_{xx}] = \nu h_x. \tag{4.5}$$

It is readily obtained that $K = d_1/(\pi\nu)$. Of course this prediction is valid in the vicinity of the origin and describes the central part of the wave. Near $|x| = (\pi/2K)$ the wave amplitude decreases to zero. Hence, the term $T_1 = 3/(2h)$ will enter in the balance to provide a transition region between the central region and the flat far-field portion. As seen from the numerical results in Figure 14, all four terms appear to be in balance in the transition region. The resolution of this behavior using matched asymptotic expansions is left for future work.

5. Conclusions. Steady gravity-capillary periodic waves on the surface of a thin viscous liquid layer coating the surface of an inclined flat plate have been investigated in the presence of an upward air stream parallel to the plate. A long-wave mathematical model was studied to describe the steady gravity-capillary waves that appear in the presence of the outer air stream. The model incorporates a nonlocal term due to the induced pressure on the liquid film by the outer air flow, as well shear stresses, gravitational forces, and surface tension. A weakly nonlinear analysis is carried out to obtain solutions to the second order in the small-amplitude parameter and to characterize the permissible steady waves. It is found that there exist two primary solution branches which are denoted as the upper and lower branches, respectively. When the surface tension becomes vanishingly small, the lower branches degenerate to the solution branches obtained by King, Tuck, and Vanden-Broeck [12], but the upper branches tend to waves of decreasing wavelength.

Extensive numerical computations are carried out to evaluate the effect of surface tension on steady state gravity waves studied by [12]. We find that surface tension provides a richer bifurcation structure and more solution branches. The first type of bifurcations is denoted by primary branches and these arise from infinitesimal linear waves that were analyzed into the weakly nonlinear regime in section 3. In the absence of surface tension, $d_2 \to \infty$ in (2.6), it is established numerically (see also [12]) that branches starting from infinitesimal waves and arbitrary values of d_1 develop nonlinearly to produce solitary wave solutions. However, when surface tension is present and for a fixed value of the air flow parameter d_1, both lower and upper solution branches will approach solitary waves only if the values of d_2 are above some critical value that depends on d_1; we found numerically and analytically that nontrivial steady waves are supported as long as $d_2 > 4d_1^2/\pi$. It is also noted that the values of d_2 above which solitary waves emerge are larger for the lower branches than the upper ones. New branches are also found whose bifurcation mechanisms are different from the primary ones. These branches bifurcate from nonlinear multimodal periodic waves. More specifically, there exist secondary bifurcation points on the primary branches, and new curves branch out from such points. Examples of bifurcations emanating from bimodal and trimodal branches have been presented.

Besides the novel bifurcation diagrams in the presence of surface tension, we also investigated the limiting configuration of the steady periodic waves in two different cases as physical parameters vary. For the first scenario we fix the value of d_1 and allow d_2 to increase so that in the limit $d_2 \to \infty$ surface tension vanishes. Our computations indicate that the wave solutions on the upper branches become narrower and almost touch the bottom, while the wave profiles on the lower branches approach the corresponding gravity solutions computed by [12]. In the second case we allow d_1 and d_2 to increase at the same time with the special ordering $d_2 = d_1^3$ motivated by the fact that for nontrivial solutions we require $d_2 \gg d_1^2$. Of course other orderings are possible, for example, $d_2 = \Gamma d_1^2$, where Γ is a sufficiently large constant, but we picked $d_2 = d_1^3$ so that the lower branch would be guaranteed to converge to the gravity solution as $d_1 \to \infty$ (in fact we assume such behavior and study limiting lower branch configurations in the absence of surface tension). Two limiting configurations are obtained. Both upper and lower branch solutions develop to almost dewetting drop-like solutions; this happens at moderate values of d_1 for the upper branch but at much higher values of d_1 for the lower branch. More precisely, it is found that the width of the profiles and the minimum wave height decrease algebraically with d_1. For the lower branch where computations could be carried out to large values of d_1, we considered the relative size of different terms in (2.6) at different positions x and found that the limiting configuration can be approximated by a cosine function in the central portion of the wave, while the flat far-field portion is described by a balance between the flux q and the wave height h through the relationship $q \sim 3h^2/2$. A transition region is required to connect the central and far-field parts of the wave, and all terms in the equation are in balance here as indicated by our computations. A matched asymptotics solution to describe this limiting behavior is the subject of ongoing work.

REFERENCES

[1] B. Akers and O. Bokhove, *Hydraulic flow through a channel contraction: Multiple steady states*, Phys. Fluids, 20 (2008), 056601.

[2] P. G. Baines and J. A. Whitehead, *On multiple states in single layer-flows*, Phys. Fluids, 15 (2003), pp. 298–307.

[3] E. S. Benilov, *Hydraulic jumps in a shallow flow down a slightly inclined substrate*, J. Fluid Mech., 782 (2015), pp. 5–24.

[4] R. Cimpeanu, S. Gomes, and D. Papageorgiou, *Active control of liquid film flows: Beyond reduced order models*, Nonlinear Dyn., 104 (2021), pp. 67–287.

[5] A. D. D. Craik, *Wind-generated waves in thin liquid films*, J. Fluid Mech., 26 (1966), pp. 369–392.

[6] E. A. Demekhin, *Nonlinear waves in a liquid film entrained by a turbulent gas stream*, Fluid Dyn., 16 (1981), pp. 188–193.

[7] T. J. Hanratty and J. M. Engen, *Interaction between a turbulent air stream and a moving water surface*, AIChE J., 3 (1957), pp. 299–304.

[8] T. J. Hanratty and A. Hershman, *Initiation of roll waves*, AIChE J., 7 (1961), pp. 488–497.

[9] H. Jeffreys and G. I. Taylor, *On the formation of water waves by wind*, Proc. Roy. Soc. A, 107 (1925), pp. 189–206.

[10] L. A. Jurman and M. J. McCready, *Study of waves on thin liquid films sheared by turbulent gas flows*, Phys. Fluids, 1 (1989), pp. 522–536.

[11] A. C. King and E. O. Tuck, *Thin liquid layers supported by steady air-flow surface traction*, J. Fluid Mech., 251 (1993), pp. 709–718.

[12] A. C. King, E. O. Tuck, and J. Vanden-Broeck, *Air-blown waves on thin viscous sheets*, Phys. Fluids, 5 (1993), pp. 973–978.

[13] C.-A. Peng, L. A. Jurman, and M. J. McCready, *Formation of solitary waves on gas-sheared liquid layers*, Int. J. Multiph. Flow, 17 (1991), pp. 767–782.

[14] Y. Taikel and A. E. Dukler, *A model for predicting flow regime transitions in horizontal and near horizontal gas-liquid flow*, AIChE J., 22 (1976), pp. 47–55.

[15] A. B. Thompson, S. N. Gomes, G. A. Pavliotis, and D. T. Papageorgiou, *Stabilising falling liquid film flows using feedback control*, Phys. Fluids, 28 (2016), 012107.

[16] R. J. Tomlin, S. N. Gomes, G. A. Pavliotis, and D. T. Papageorgiou, *Optimal control of thin liquid films and transverse mode effects*, SIAM J. Appl. Dyn. Syst., 28 (2019), pp. 117–149.

[17] D. Tseluiko and S. Kalliadasis, *Nonlinear waves in counter-current gas–liquid film flow*, J. Fluid Mech., 673 (2011), pp. 19–59.

[18] D. Tseluiko and D. Papageorgiou, *Wave evolution on electrified falling films*, J. Fluid Mech., 556 (2006), pp. 361–386.

[19] E. O. Tuck, *On air flow over free surfaces of stationary water*, J. Austral. Math. Soc. Ser. B, 19 (1975), pp. 66–80.

[20] E. O. Tuck and J. Vanden-Broeck, *Influence of surface tension on jet-stripped continuous coating of sheet materials*, AIChE J., 30 (1984), pp. 808–811.

[21] M. Van Dyke, *Perturbation Method in Fluid Mechanics*, Academic Press, New York, 1964.